

Development of Ferrite-Based Temperature Sensors for Magnetic Resonance Imaging: A Study of $\text{Cu}_{1-x}\text{Zn}_x\text{Fe}_2\text{O}_4$

N. A. Alghamdi,^{1,*} J. H. Hankiewicz,¹ N. R. Anderson,¹ K. F. Stupic,²
R. E. Camley,¹ M. Przybylski,^{3,4} J. Żukrowski,⁴ and Z. Celinski¹

¹*UCCS BioFrontiers Center, University of Colorado,*

Colorado Springs 1420 Austin Bluffs Parkway, Colorado 80918, USA

²*National Institute of Standards and Technology, Boulder, Colorado 80305, USA*

³*Academic Centre for Materials and Nanotechnology,*

AGH University of Science and Technology, 30-059 Krakow, Poland

⁴*Faculty of Physics and Applied Computer Science, AGH University of Science and Technology,
30-059 Krakow, Poland*



(Received 12 July 2017; revised manuscript received 5 March 2018; published 21 May 2018)

We investigate the use of $\text{Cu}_{1-x}\text{Zn}_x\text{Fe}_2\text{O}_4$ ferrites ($0.60 < x < 0.76$) as potential sensors for magnetic-resonance-imaging thermometry. Samples are prepared by a standard ceramic technique. Their structural and magnetic properties are determined using x-ray diffraction, scanning electron microscopy, superconducting quantum-interference device magnetometry, and Mössbauer and 3-T nuclear-magnetic-resonance spectroscopies. We use the mass magnetization of powdered ferrites and transverse relaxivity r_2^* of water protons in Ringer's-solution-based agar gels with embedded micron-sized particles to determine the best composition for magnetic-resonance-imaging (MRI) temperature sensors in the (280–323)-K range. A preclinical 3-T MRI scanner is employed to acquire T_2^* weighted temperature-dependent images. The brightness of the MRI images is cross-correlated with the temperature of the phantoms, which allows for a temperature determination with approximately 1 °C accuracy. We determine that the composition of $0.65 < x < 0.70$ is the most suitable for MRI thermometry near human body temperature.

DOI: [10.1103/PhysRevApplied.9.054030](https://doi.org/10.1103/PhysRevApplied.9.054030)

I. INTRODUCTION

Localized temperature is an important parameter that describes the health status of an individual during a medical diagnosis or treatment. It can reflect multiple health issues such as the presence of inflammation or tumors [1,2]. To determine the temperature deep in the body, one may use an invasive probe that delivers a single reading [3–5] or noninvasive technique such as magnetic-resonance-imaging (MRI)-based thermometry that can provide temperature maps. Such maps, in contrast to single-point measurements, are useful during certain MRI-guided procedures, such as thermal treatments (e.g., ablation [6] or hyperthermia [7]). During these procedures, the temperature is monitored to protect healthy tissue from damage and to ensure that the treated part is sufficiently heated.

Several MRI-based methods have been developed to measure local body temperature [8,9]. Intrinsic properties such as the spin-lattice relaxation time, T_1 , the spin-spin relaxation time, T_2 , and the diffusion coefficient of water molecules have been suggested as a method for determining temperature [10]. Currently, the most popular method for

MRI-based thermometry involves measuring the proton-resonance frequency (PRF) shift [11,12]. This method gives an accuracy of approximately 1 °C in nonmoving tissues [13]. PRF may also be used for *in vitro* applications to monitor the temperature inside cell cultures [14]. However, this method has certain limitations. PRF does not work with adipose tissue and is very sensitive to body movement (cardiac and/or respiratory) [15]. These issues can be partially mitigated with the referenceless PRF method [16]. In addition, the phase component of the image strongly depends on the stability and homogeneity of the static magnetic field B_0 . Although, in recent studies, the effect of the magnetic-field drift has been reduced, field inhomogeneity remains a significant obstacle in MRI thermometry [17].

Recently, we proposed the use of an exogenous agent in the form of magnetic particles suitable for MRI thermometry [18]. If the magnetic moment of magnetic particles is temperature dependent, this magnetic moment creates a temperature-variable inhomogeneous local magnetic field leading to nuclear-magnetic-resonance (NMR) line-width and MRI intensity changes as a function of temperature. Preliminary results using Gd particles allowed us to produce a temperature-dependent MRI image. Employing the MRI image signal (i.e., the brightness), we could

*Corresponding author.
n-phys@hotmail.com

determine the temperature with 1 °C accuracy. However, Gd alone is toxic and is only used in clinical settings if appropriately sequestered [19]. We have already investigated the possibility of using iron-based oxides (ferrites) as more biocompatible materials for designing MRI temperature sensors [20]. Studies on a CuZn ferrite reported a toxicity slightly above Fe₃O₄, and close to that of Fe₂O₃. The same work indicated some DNA damage in cells exposed to the CuZn ferrite [21].

Lately, ferrites have experienced an application renaissance due to the combination of their unique magnetic and electrical properties, as well as very high chemical and mechanical stability. Besides their traditional uses as magnetic storage media and in telecommunications, ferrites are used as gas, stress, bio-, and humidity sensors [22–26]. In this paper, we present systematic studies of Cu_{1-x}Zn_xFe₂O₄ ferrite particles to be used as temperature-dependent MRI sensors. Our objective is to determine the optimum composition for this class of agents suitable for the detection of temperature changes in a range near human body temperature. Below, we provide a detailed description of the experimental results we use to select the best candidate materials for MRI thermometry.

II. SAMPLE PREPARATION AND CHARACTERIZATION METHODS

Samples of Cu_{1-x}Zn_xFe₂O₄ ferrites are prepared with a standard ceramic technique [27,28]. Ferrite compositions of 0.60 < x < 0.76 are used in the NMR and MRI measurements. Samples with compositions $x = 0, 0.4, 0.65,$ and 1 are prepared for the Mössbauer spectroscopy studies. CuO, ZnO, and Fe₂O₃ powders are mixed with an appropriate stoichiometry in isopropanol. The oxide mixture is ball milled for 18 h, and the slurry is then dried and pressed into disk-shaped samples. Samples are presintered at 970 °C for 9 h and calcined at 1130 °C for 4 h. The resulting ferrites are crushed using a mortar and pestle for either about 10 min to be studied by x-ray diffraction (XRD) and Mössbauer spectroscopy or for 2 h to be studied in NMR and MRI experiments. The ferrite structure is determined using an XRD system with Cu K_{α} radiation ($\lambda = 1.5406$ Å). All of the XRD measurements are carried out using the Bragg-Brentano geometry with a monochromator in front of the detector. A scanning electron microscope (SEM) equipped with energy-dispersive spectroscopy is employed to confirm the sample composition and monitor the size distribution of particles in the powders used in the NMR and MRI experiments.

The magnetic properties are determined using a superconducting quantum-interference device (SQUID) magnetometer. All of the reported measurements are carried out on a bulk piece of the ferrite sample (approximately 2 mg of weight). The measurements are conducted in field-cooled fashion; i.e., samples are cooled to 4 K while in a 5-T field. Temperature-dependent measurements of mass

magnetization are carried out at desired field values (0.002, 0.02, 0.364, 3.0, and 5.0 T) in the temperature range of 4 to 350 K.

Mössbauer ⁵⁷Fe spectra are measured by recording 7.3 keV conversion electrons (conversion electron Mössbauer spectroscopy mode) at different temperatures (from 6 to 300 K) in zero magnetic field, after magnetizing the samples in a strong magnetic field. Spectra are collected using a standard spectrometer working in a constant acceleration mode for all samples. Further experimental details are found in Przybylski *et al.* [29].

For NMR measurements, samples consisted of Cu_{1-x}Zn_xFe₂O₄ ferrite particles suspended in 2% Ringer’s-solution-based agar gels with a concentration of 3.5 mM for $x = 0.65, 0.68, 0.70,$ and 0.73 . Compositions of $x = 0.60$ and 0.76 are not studied due to a high initial value of mass magnetization and a slow decrease of magnetization near targeted temperature (310 K), respectively, as described in the following sections. Measurements of temperature-dependent linewidth and nuclear relaxation times T_1 (inversion-recovery method) and T_2 (Carr-Purcell-Meiboom-Gill sequence) are performed at 364 mT. For r_2^* , determination of the NMR linewidth at FWHM is calculated from the free-induction-decay Fourier transform obtained after a 2- μ s hard rf pulse.

The observed experimental linewidth is converted to relaxivity r_2^* using a known formula [30]: $r_2^* = \{[1/(T_{2\text{matrix+particles}}^*)] - [1/(T_{2\text{matrix}}^*)]\} / C$, where $(1/T_{2\text{matrix}}^*)$ is the relaxation rate of the diamagnetic host (agarose) and $(1/T_{2\text{matrix+particles}}^*)$ is the relaxation rate of the host with ferrite particles of concentration C in mM. The ¹H NMR linewidth $\nu_{1/2}$ is related to T_2^* by $\nu_{1/2} = [1/(\pi T_2^*)]$ [31].

Temperature-dependent MR images of a prepared phantom are obtained from a MRI preclinical scanner equipped with a 3.0-T, 30-cm-bore superconducting magnet. The phantom consists of three cylindrical plastic cryogenic vials (10-mm inner diameter and 80-mm length). One vial is filled with a pure 2% Ringer’s-solution-based agar gel. The other two vials are filled with 1 and 0.5 mM of three different compositions of Cu_{1-x}Zn_xFe₂O₄ ferrite ($x = 0.65, 0.70,$ and 0.73) dispersed in a 2% Ringer’s-solution-based agar gel. Each tube has three different ferrite composition zones. The details of the phantom preparation protocol were described earlier [17]. The phantom is placed in a custom-built temperature-controlled cell shown in the Fig. 1. The temperature of the cell is controlled using a standard bath circulator with a continuous flow of protonless perfluorocarbon (PFC) coolant to eliminate extraneous ¹H signals from the MR images. The temperature of the samples is monitored by a fiber-optic sensor placed at the center of the temperature cell. Temperature data are acquired every 5 s throughout the imaging experiment. The gradient-echo method, sensitive to local magnetic-field inhomogeneity [32–34], is employed for imaging using the following parameters: slice orientation, axial; field of

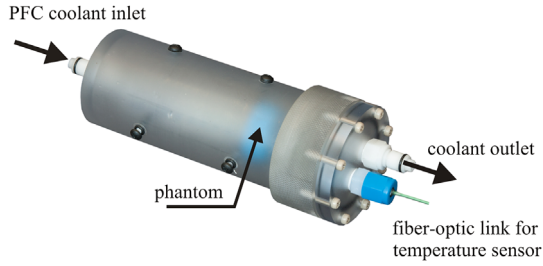


FIG. 1. Temperature-controlled cell for a temperature-dependent MRI. The picture shows only one sensor attached, although up to four sensors can be inserted.

view, $30 \times 30 \text{ mm}^2$; matrix, 64×64 (in-plane resolution, -0.47 mm/pixel); slice thickness, 4 mm ; repetition time, -100 ms ; echo time, -2.52 ms ; and radio-frequency flip angle, -20° .

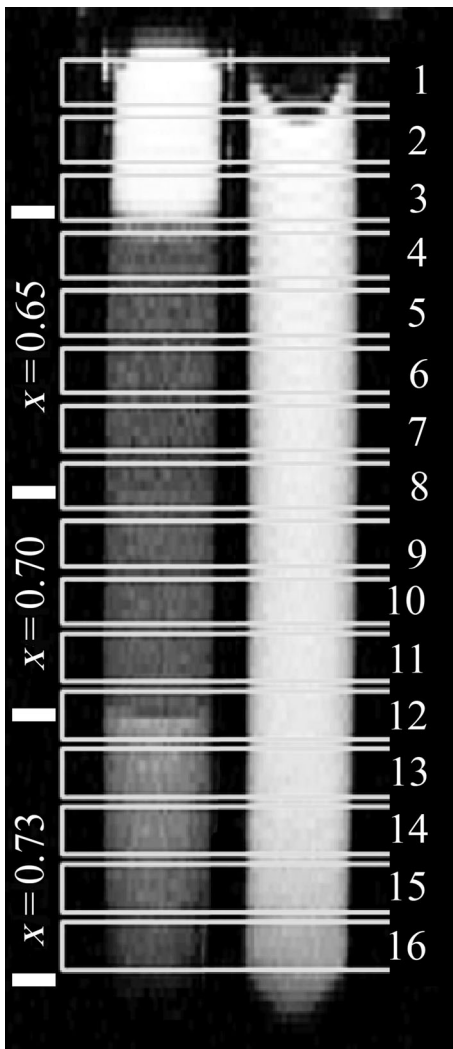


FIG. 2. The coronal image of the phantom used for positioning of the axial slices. (Right) Pure 2% Ringer's-solution-based agar gel. (Left) 0.5-mM concentration of $\text{Cu}_{1-x}\text{Zn}_x\text{Fe}_2\text{O}_4$ particles in a Ringer's-solution-based agar gel. The top of the vial on the left is terminated with pure agar gel.

Figure 2 shows the coronal image used to navigate to locations of axial images. The right vial is filled with a pure 2% Ringer's-solution-based agar gel, which is used as a control sample. The left tube consists of agar gel with embedded $\text{Cu}_{1-x}\text{Zn}_x\text{Fe}_2\text{O}_4$ ferrite particles with different compositions of $x = 0.73, 0.70,$ and 0.65 from the bottom, respectively. The location of different compositions in Fig. 2 is easily distinguished by different brightnesses, as the image is T_2^* weighted. The concentration of ferrite particles in this tube is 0.5 mM . In the image analysis, the intensities of three axial slices within each composition are added to obtain the mean intensity value and the standard deviation. Axial images are averaged over the entire tube cross section. The following slices are used: (a) the concentration $x = 0.65$ uses slices 5, 6, and 7; (b) the concentration $x = 0.70$ uses slices 9, 10, and 11; and (c) the concentration $x = 0.73$ uses slices 13, 14, and 15.

III. RESULTS AND DISCUSSION

A. Structural characterization

The XRD measurements confirm the formation of a single $\text{Cu}_{1-x}\text{Zn}_x\text{Fe}_2\text{O}_4$ crystallographic phase ($Fd\bar{3}m$, space group 227). Figure 3 shows a typical XRD pattern for prepared ferrite samples obtained specifically for $\text{Cu}_{0.35}\text{Zn}_{0.65}\text{Fe}_2\text{O}_4$ composition with the green solid bars of copper zinc ferrite obtained from Ref. [35]. The determined lattice constant, a , is 8.4021 \AA for $x = 0.65$. However, the measured relative intensities differ for some (hkl) peaks, indicating that the distribution of Cu and Zn atoms in the Fe sites is different from those reported in the literature for these ferrites [22].

SEM is employed to determine the size distribution of the particles used in our NMR and MRI studies. The inset in Fig. 4 shows a typical SEM image of the particles dispersed on the surface of a Si wafer covered with Pt. Image analysis allows us to obtain histograms of the major

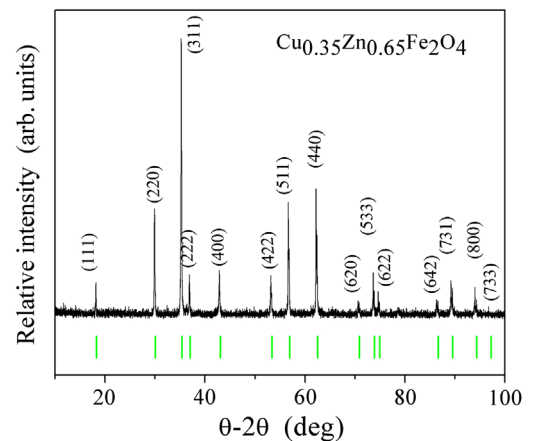


FIG. 3. XRD pattern of the ferrite powder sample in the $\text{Cu}_{0.35}\text{Zn}_{0.65}\text{Fe}_2\text{O}_4$ composition. Solid green bars represent the corresponding positions of the peaks from Ref. [35].

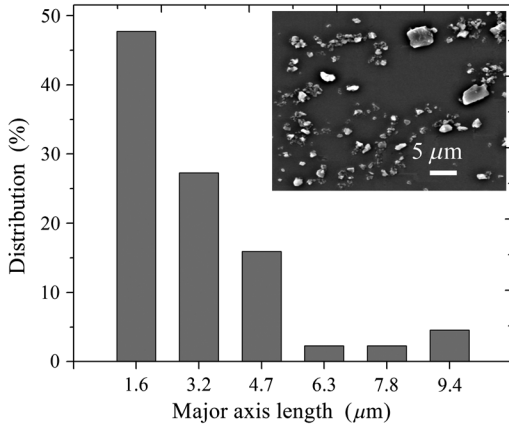


FIG. 4. Histogram of a particle-size distribution for the $\text{Cu}_{0.27}\text{Zn}_{0.73}\text{Fe}_2\text{O}_4$ sample obtained from the SEM image shown in the inset.

axis length for the measured powders. We estimate the median value at $2.38 \mu\text{m}$. Figure 4 shows an example of such a histogram for the $\text{Cu}_{0.27}\text{Zn}_{0.73}\text{Fe}_2\text{O}_4$ sample.

B. SQUID magnetometry

Figure 5(a) displays an example of the temperature dependence of the mass magnetization measurements using a SQUID magnetometer at selected fields for the $\text{Cu}_{0.35}\text{Zn}_{0.65}\text{Fe}_2\text{O}_4$ sample. Other measured ferrite samples exhibit a similar qualitative behavior. In high applied magnetic fields (3 and 5 T), the magnetization is a linear

function of temperature above 150 K. A rapid decrease of magnetization with increasing temperature above 150 K is also observed for measurements carried out in a 364-mT field. This effect is important because we perform NMR studies at 364 mT applied field. As discussed later, the temperature-dependent changes of the water proton transverse relaxivity r_2^* , and the image intensity of the phantoms in MRI studies will be correlated with changes of magnetization of particles embedded in prepared phantoms. The data in Fig. 5(a) clearly indicates that, as the applied field increases, the transition to the paramagnetic state shifts to higher temperatures. The measurements of the temperature dependence of the magnetization at low applied fields (2 and 20 mT) exhibit very different behavior. The magnetization is almost constant over a large temperature range and decreases rapidly near the Curie transition temperature, T_C .

Figure 5(b) displays the temperature dependence of the mass magnetization measured in the field of 2 mT for different ferrite samples. Using these data, we determine the T_C value for the different compositions using an approach, based on the expansion of the free energy near T_C , that is described in detail by Fabian *et al.* [36].

Figure 5(c) shows T_C as a function of the composition, the values of which we obtain by an analysis of the data shown in Fig. 5(b). The Curie temperature decreases almost linearly with increasing Zn concentration. The determined T_C values are also listed in Table I. The presented results are in agreement with earlier experimental reports [21,37], as well as theoretical predictions [38].

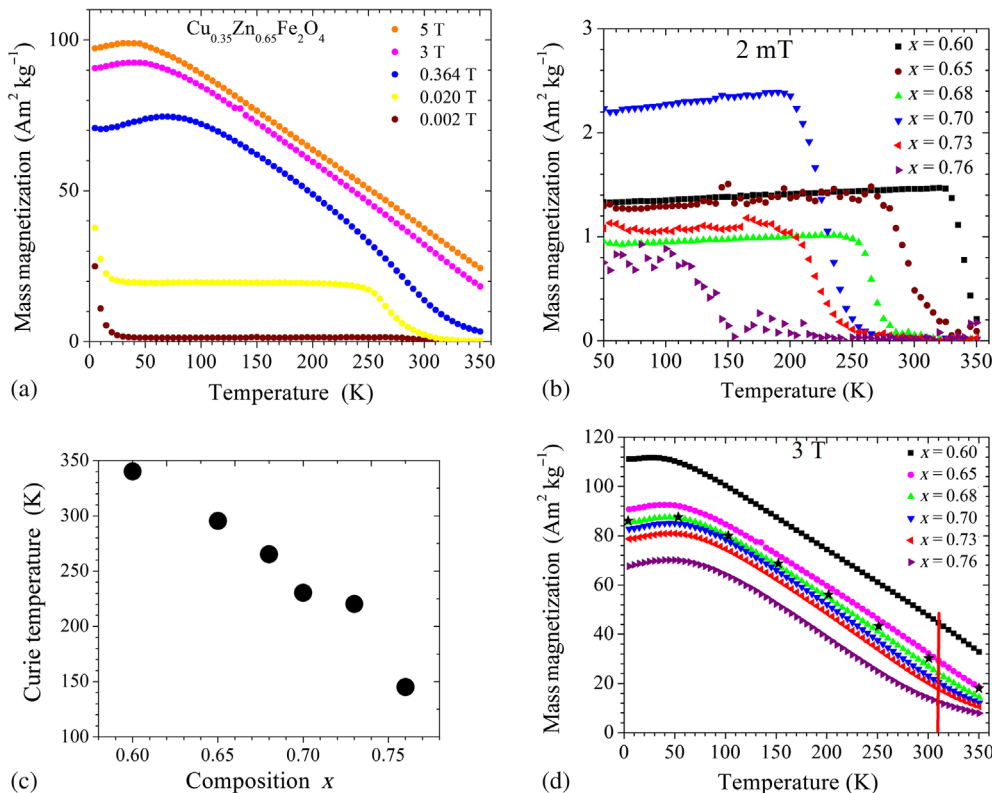


FIG. 5. (a) Temperature-dependent mass magnetization of $\text{Cu}_{0.35}\text{Zn}_{0.65}\text{Fe}_2\text{O}_4$ measured in different magnetic fields for the bulk sample. (b) Temperature-dependent mass magnetization measured in 0.002 T for different ferrite compositions. (c) Curie transition temperature, T_C , as a function of composition. (d) Temperature-dependent mass magnetization at 3 T for different ferrite compositions. The black stars in Fig. 5(d) represent mass magnetization measured for micrometer-sized particles for $x=0.68$. The red line shows the human body temperature (37.0°C).

TABLE I. Summary of analysis of $\text{Cu}_{1-x}\text{Zn}_x\text{Fe}_2\text{O}_4$ ferrite samples. T_C , Curie temperature; dM_m/dT , slope of the mass magnetization as a function of temperature calculated in the temperature range 280–333 K in an applied field of 3 T; M_m , mass magnetization at 310 K in an applied field of 3 T; $[(dr_2^*)/(dT)]$, slope of the proton transverse relaxivity r_2^* as a function of temperature in the temperature range 280–323 K in an applied field of 364 mT; Pearson correlation coefficient calculated between the mass magnetization and experimental r_2^* data for measurements taken in an applied field of 364 mT. NMR in agar gel with embedded particles of composition $x = 0.60$ and 0.76 is not carried out due to the high value of the mass magnetization ($44 \text{ A m}^2 \text{ kg}^{-1}$) and the slow decrease of magnetization vs temperature ($-0.15 \text{ A m}^2 \text{ kg}^{-1} \text{ K}^{-1}$), respectively.

x	T_C (K)	dM_m/dT $H = 3$ T ($\text{A m}^2 \text{ kg}^{-1} \text{ K}^{-1}$)	M_m $H = 3$ T at 310 K ($\text{A m}^2 \text{ kg}^{-1}$)	$[(dr_2^*)/(dT)]$ $H = 364$ mT ($\text{s}^{-1} \text{ mM}^{-1} \text{ K}^{-1}$)	Pearson coefficient
0.60	340	-0.285 ± 0.001	44		
0.65	295	-0.287 ± 0.001	29	-9.39 ± 0.58	0.99
0.68	265	-0.276 ± 0.002	24	-7.46 ± 0.36	0.99
0.70	230	-0.261 ± 0.004	20	-4.72 ± 0.24	0.99
0.73	220	-0.234 ± 0.004	17	-2.36 ± 0.39	0.91
0.76	145	-0.150 ± 0.003	12		

Figure 5(d) summarizes the temperature dependence of the mass magnetization at 3 T for all samples with different Zn concentrations. While the magnetization decreases with increasing temperature for all of the measured samples between 280 and 333 K, the largest slope is observed for samples with $x = 0.6$ and 0.65 . The slope values (dM/dT) in this temperature region are listed in Table I. We note that the change in the mass magnetization with temperature, at 3 T, for the $\text{Cu}_{0.35}\text{Zn}_{0.65}\text{Fe}_2\text{O}_4$ ferrite is similar to that obtained for micron-sized metallic Gd particles ($-0.287 \pm 0.001 \text{ A m}^2 \text{ kg}^{-1} \text{ K}^{-1}$ and $-0.278 \pm 0.008 \text{ A m}^2 \text{ kg}^{-1} \text{ K}^{-1}$, respectively), indicating that the ferrites may be a reasonable, and more biocompatible, alternative to Gd for MRI thermometry [18]. We also note that measurements performed on micrometer-sized particles confirmed that they exhibit magnetic properties similar to the properties of bulk materials. For the composition $\text{Cu}_{0.32}\text{Zn}_{0.68}\text{Fe}_2\text{O}_4$, we perform measurements using bulk (green triangles) and powder (black stars) samples with micrometer-sized particles [see Fig. 5(d)]. The agreement is remarkable.

While the presented structural and magnetometry results are for micron-sized particles or bulk materials, we recognize that, in order to use these ferrites as intravenously administered, contrast in MRI thermometry nanoparticles has to be used. Our initial results indicate that fabrication of nanosized ferrite particles can be accomplished by using a colloidal method [39,40].

C. Mössbauer spectroscopy

To understand the substitution of Zn and Cu atoms into two different sublattices of the Fe_3O_4 structure and the resulting magnetic properties of the $\text{Cu}_{1-x}\text{Zn}_x\text{Fe}_2\text{O}_4$ ferrites, we perform Mössbauer ^{57}Fe spectroscopy measurements. Owing to the scope of this paper, here we highlight only the most important conclusions and show the evolution of the measured spectra at selected temperatures for

$x = 0.65$ of our Mössbauer studies (see Fig. 6). The detailed analysis will be presented in an upcoming paper. We note that similar results, focusing primarily on room-temperature measurements for bulk samples, were published earlier [41,42].

Because there are two Fe positions (tetrahedral and octahedral) in the spinel structure, at least two components should be expected in the Mössbauer spectra. Fe atoms occupying octahedral sites are antiferromagnetically coupled to Fe atoms occupying tetrahedral sites. Their occupation should follow a ratio of 2:1; however, the site occupation is more complicated because the octahedral positions are occupied by both Me^{2+} and Fe^{3+} cations. We note that, at room temperature, the spectra of the samples with $x > 0.4$ exhibit a relaxation character.

Room-temperature measurements are done at zero external magnetic field and at 300 K, where there is no net magnetization. Thus, the standard six-peak Fe spectrum is not observed (see the top panel of Fig. 6). Moreover, the relaxation spectra do not show well-defined discrete components that can be attributed to Fe atoms in different crystallographic sublattices.

The magnetization relaxation is fully suppressed only at 6 K, and a well-defined magnetic splitting is observed. Therefore, only low-temperature (6-K) spectra are analyzed, employing the Voigt-based method proposed by Rancourt and Ping [43,44]. The spectra are assumed to be a sum of two components (octahedral and tetrahedral sublattices) with Gaussian magnetic hyperfine parameter distributions and the relative contributions of both the components to be closed to a 72:28 ratio. The average magnetic hyperfine field, B_{hf} , of 510.1 kG corresponding to both the components (512 and 506 kG) is similar to the average B_{hf} of 510 kG measured for Fe_3O_4 [45] at 6 K, and it is only weakly dependent on x . This weak dependence of B_{hf} on x means that the substitution of Fe for Cu and Zn does not change the average magnetic hyperfine field at the

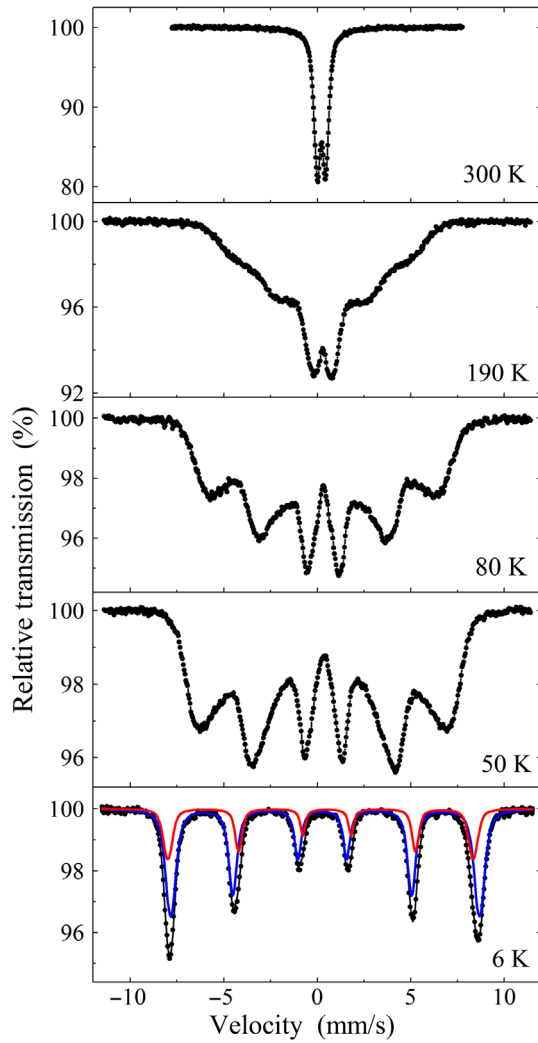


FIG. 6. The Mössbauer ^{57}Fe spectra at different temperatures for $x = 0.65$.

Fe nuclei significantly. Isomer shifts for both components are large, suggesting that there are Fe^{3+} atoms in both sublattices. From our analysis of the spectra for $x = 0.4$ and 0.65 we conclude that, for increasing x values, Cu and Zn atoms are preferentially substituted into the octahedral sites. As a result, the net magnetic moment, i.e., $M_B - M_A$ decreases in agreement with the SQUID measurements.

D. NMR spectroscopy

As expected for such large particles, very low values of longitudinal relaxivity r_1 are obtained. For all compositions and concentrations measured in the temperature range of 5°C to 50°C , r_1 is less than $0.2 \text{ s}^{-1} \text{ mM}^{-1}$. Figure 7 shows the results of nuclear transverse relaxivity r_2^* . The r_2^* value clearly exhibits a significant monotonic temperature dependence. These results are consistent with the SQUID measurements showing a reduction of magnetization with temperature. We correlate the measured

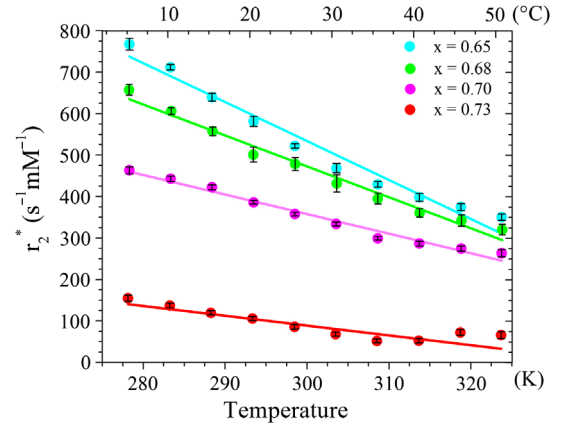


FIG. 7. Temperature dependence of transverse nuclear relaxivity r_2^* . The solid lines represent linear regression (see Table I for a list of the slope values).

temperature-dependent r_2^* value with the temperature-dependent mass magnetization at a field of 364 mT (see the calculated Pearson correlation coefficients in Table I). All samples show high correlation, larger than 0.9 , between the mass magnetization and r_2^* . Moreover, we note that r_2^* decreases with an increasing Zn concentration (see Fig. 7 and Table I).

A similar value of transverse relaxivity of approximately $500 \text{ s}^{-1} \text{ mM}^{-1}$ is obtained at room temperature for 100-nm iron oxide clusters at 7.0 T [46], compared to $550 \text{ s}^{-1} \text{ mM}^{-1}$ at 364 mT in this study of copper zinc ferrites. We note that the authors in the aforementioned study intentionally used clustering of magnetic nanoparticles in the shape of large and low-symmetry aggregates to enhance r_2 relaxivity. This clustering makes particles more efficient as a contrast agent in detecting cancer in the mouse model of a liver tumor.

The rapid decrease of r_2^* with increasing temperature suggests a possible temperature-dependent change in the brightness of the T_2^* -weighted MRI images. In Table I, we list slopes of the linewidth broadening in the temperature range $278\text{--}323 \text{ K}$. From these data, we conclude that the best ferrite composition to use for imaging is around $x = 0.65\text{--}0.68$. This composition range has a relatively high temperature dependence on the linewidth broadening and small value of mass magnetization at 323 K . As a result, one may expect bright MR images to be useful for the determination of temperature changes.

To understand the r_2^* vs temperature curves, we perform calculations for the NMR linewidth broadening that is expected from a distribution of $2.4\text{-}\mu\text{m}$ -diameter ferrite particles, based on the following method [17]. Because of the large particle size, we are in the static dephasing regime, far from the narrowing conditions, where the diffusion of water molecules may be neglected [47–50]. For the linewidth calculation, a sample volume is created based on the concentration of ferrite particles in solution assuming no

agglomeration of particles. The volume is then partitioned into a three-dimensional grid of cells with a side length of $0.1 \mu\text{m}$. A ferrite particle is placed at the center of the volume and given a magnetization based on experimental measurements. The inhomogeneous field from the magnetic particle is calculated for each point in the grid and then added to the static field to determine the total magnetic field for each grid point in the sample volume. This distribution of magnetic-field values is then multiplied by the proton gyromagnetic ratio to get a frequency spectrum, which allows us to calculate a linewidth. Then the temperature of the system is changed and the calculation is performed again. Our calculation of linewidth uses the measured magnetization as a function of temperature and the average particle size and does not contain any arbitrary fitting parameters.

A comparison of experimental results vs theoretical calculations is shown in Fig. 8. As can be seen, the magnitude of the experimental and theoretical results varies; however, the slope of both sets of curves is consistent up to 310 K. We note that bigger values of linewidth broadening for experimental data than the theoretical calculations may originate from the wide dispersion of particle sizes in the samples. The variety of sizes and shapes can increase local magnetic-field inhomogeneity due to reduced dipolar field symmetry [39]. This effect eventually leads to an increase of the linewidth from water protons in agar gel with embedded particles. We hypothesize here that less monodisperse and less symmetrical particles will produce, in general, a more efficient r_2^* contrast agent for MR imaging. The slope of r_2^* vs temperature is the determining factor in the MRI temperature measurements, and we use it as a guide in our selection of the best ferrite composition. This method shows that the $\text{Cu}_{0.35}\text{Zn}_{0.65}\text{Fe}_2\text{O}_4$ composition displays the steeper slope necessary for MRI thermometry (Table I).

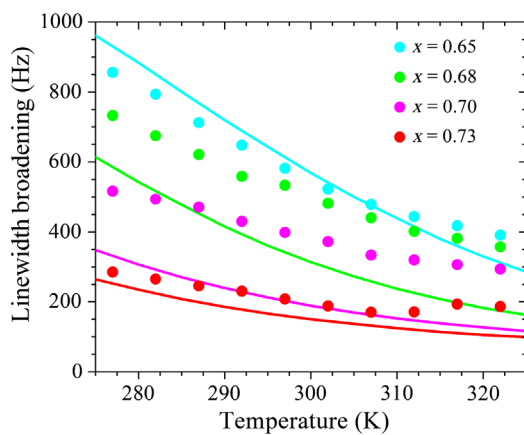


FIG. 8. Experimental results (symbols) compared to theoretical calculations (the solid lines) for the NMR linewidth as a function of temperature for four different compositions.

E. MR imaging

Temperature-dependent MR images are acquired using a Ringer's-solution-based agar gel phantom for the three most promising compositions of $\text{Cu}_{1-x}\text{Zn}_x\text{Fe}_2\text{O}_4$ ferrite particles of $x = 0.65, 0.70,$ and 0.73 , as described in the sample preparation and characterization method section above. Figure 9 shows MRI axial images of the phantom at three selected temperatures, where the brightness of the MR images increases with temperature. In addition to the temperature changes in the image brightness, we also observe the influence of the ferrite composition and the molar concentration of magnetic particles on the MRI brightness. In the extreme case at 4.3°C , the image of $x = 0.65$ in a 1-mM concentration is hardly visible due to the particles' high magnetization at this temperature [see Fig. 5(d)] and, consequently, the highest NMR line broadening (see Fig. 7).

Figures 10(a) and 10(b) depict the temperature dependence of the relative image intensity (the ratio of image intensity of pure agar gel to the image intensity of gel doped with ferrite particles) measured in the MRI experiments for different ferrite particle concentrations (0.5 and 1 mM , respectively). The relative intensity of the images decreases linearly with temperature, and it is more pronounced for 1-mM ferrite particle concentration. This behavior is complementary to the observed behavior from the SQUID magnetometry, the NMR linewidth measurements, and theoretical calculations of the NMR linewidth. The analysis of the MR image intensity confirms the methodology for selection of the composition of the ferrite temperature contrast agent.

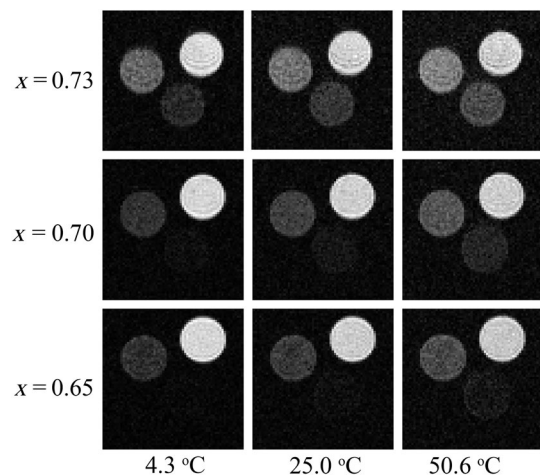


FIG. 9. MR images of a phantom at three different temperatures for different compositions of ferrite: $x = 0.73, 0.70,$ and 0.65 . Each square is a (3×3) -cm image of the phantom. In the top right corner of each square is the pure-agar-gel reference sample. In the top left is the agar gel with a 0.5-mM concentration of ferrite particles. At the bottom is the agar gel with a 1-mM concentration of particles.

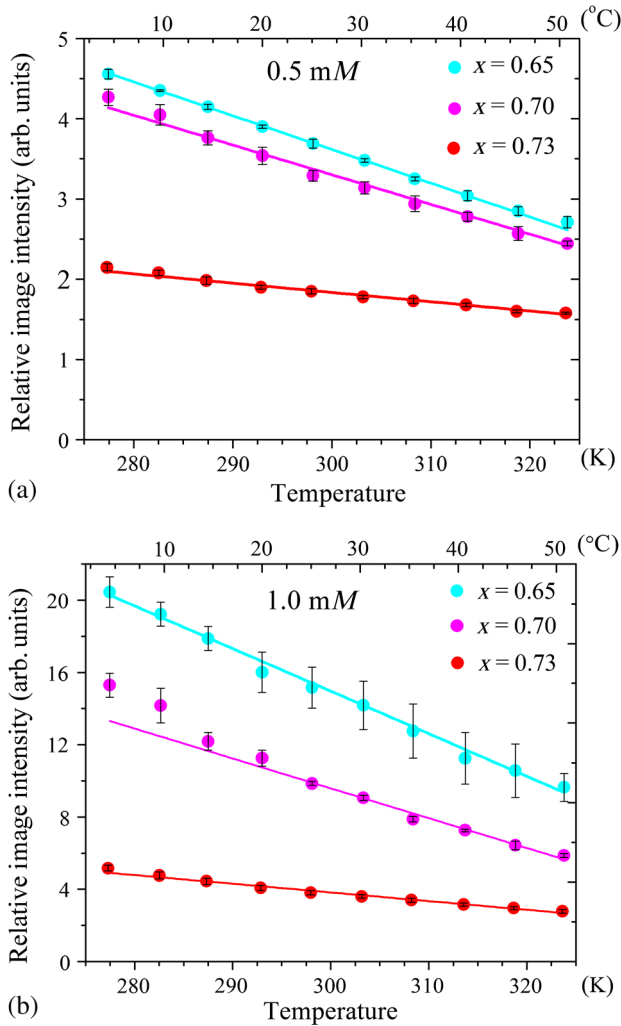


FIG. 10. Temperature dependence of the relative image intensity for different compositions of ferrite particles and for different concentrations. (a) 0.5 mM. (b) 1-mM. The solid lines represent the linear fit to our data (see the slope values in Table II).

The relative image intensity of the phantom is analyzed at temperatures ranging from 4.3 $^{\circ}\text{C}$ to 50.6 $^{\circ}\text{C}$ using a linear regression to obtain intensity vs temperature slopes and 95% confidence bands. Numerical values of slopes are given in Table II. Regression slopes and confidence bands similar to those described earlier are used to determine the temperature accuracy [17]. Figure 11 shows a summary of

TABLE II. Slopes of MR image brightness (dI_r/dT) as a function of temperature measured at an applied field of 3 T for 0.5- and 1-mM concentrations of $\text{Cu}_{1-x}\text{Zn}_x\text{Fe}_2\text{O}_4$ particles.

x	dI_r/dT	
	0.5 mM	1.0 mM
0.65	-0.042 ± 0.001	-0.236 ± 0.018
0.70	-0.037 ± 0.001	-0.165 ± 0.004
0.73	-0.012 ± 0.001	-0.048 ± 0.002

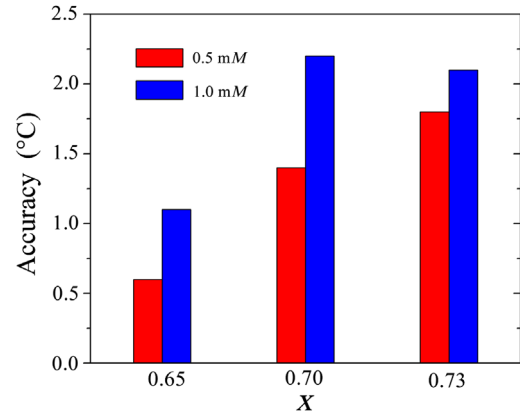


FIG. 11. Temperature accuracy as a function of x for different compositions of $\text{Cu}_{1-x}\text{Zn}_x\text{Fe}_2\text{O}_4$ ferrite ($x = 0.65, 0.70,$ and 0.73) embedded in 0.5- and 1.0-mM molar concentrations of Ringer's-solution-agar gel. The best accuracy is found for $x = 0.65$ and a concentration of 0.5 mM.

the temperature determination accuracy at 37 $^{\circ}\text{C}$, i.e., near human body temperature. For both concentrations of particles, the best accuracy is obtained for the composition characterized by the fastest magnetization drop ($x = 0.65$), as predicted in the analysis of the SQUID and NMR results. However, the 1-mM-concentration samples show worse accuracy than the 0.5-mM ones. This happens due to the short T_2^* value and, consequently, a drastic drop of the signal-to-noise ratio (SNR) for images with the 1-mM concentration of ferrite. The above observation emphasizes the importance of a fast magnetization reduction in the thermal region of interest, and of a high SNR from ^1H in water in designing magnetic contrast agents for MRI thermometry and will be a subject of further investigation.

F. Particle stability

We test the particle stability of the $\text{Cu}_{0.35}\text{Zn}_{0.65}\text{Fe}_2\text{O}_4$ composition in dry form and in aqueous solutions. Samples of a 2% agar Ringer's-solution gel with particles are tested for relaxivity R_2^* immediately after fabrication and after 8 months of storage at 4 $^{\circ}\text{C}$. We notice only a 5% decrease of R_2^* between 5 $^{\circ}\text{C}$ and 50 $^{\circ}\text{C}$, a range within the experimental error of our setup. The same composition stored at room temperature in the dry form for 20 months shows only a 3.6% drop of mass magnetization when measured with a SQUID.

We conclude that ferrite particles are very stable in aqueous solutions with a well-preserved original magnetization that is necessary for an accurate temperature determination.

G. Particle toxicity

Preliminary toxicity studies are conducted on particles made of $\text{Cu}_{0.35}\text{Zn}_{0.65}\text{Fe}_2\text{O}_4$. Henrietta Lacks cervical-cancer cells are seeded on to well plates with a

poly-L-lysine treatment to improve cell adherence. Cells are seeded at 50 000 cells per well, in accordance with the layouts. Particles are then added in varying concentrations from 0.1 to 10 mM and incubated for 8 h at 37 °C. A working concentration of 1-mM is also applied to several plates that are incubated at increasing times (1, 2, 4, 8, and 24 h). Postincubation cell plates are then washed with $1\times$ phosphate-buffered saline to rid them of any extra nanoparticles. Cells are then fixed with a 2% formaldehyde solution to prevent decay, terminate ongoing biochemical reactions, and preserve the cells for analytical staining. We then apply a 30- μ M 4', 6-diamidino-2-phenylindole (DAPI) stain which binds to the DNA of fixed cells and gives off fluorescence readings of 358-nm excitation and 461-nm emission. Cell plates are then read on a plate reader, with filters set to DAPI's fluorescence. These readings of the cells are then recorded and compared to the untreated cell wells to assess the viability of the cells and, therefore, the toxicity of the particles.

We see from the 8 h concentration curve assay that the DAPI data show that particles display a slight increase in toxicity (lower cell viability) with an increase in concentration. The 1-mM working concentration is around 80% viable. However, cell viability does not fall below 60%, even after a 24-h time of incubation.

IV. CONCLUSIONS

In conclusion, $\text{Cu}_{1-x}\text{Zn}_x\text{Fe}_2\text{O}_4$ ferrites in the form of small particles can be employed as sensors in MRI thermometry. With an appropriate doping of metallic cations, one can control the transition temperatures of ferrites and therefore shift the sensitivity to the temperature region of interest imaged by MRI. In this paper, we target the temperature region near human body temperature. We demonstrate that micrometer-sized magnetic particles made of the $\text{Cu}_{0.35}\text{Zn}_{0.65}\text{Fe}_2\text{O}_4$ ferrite allows for a MRI determination of the temperature with an accuracy of ± 0.6 °C at a temperature of 37 °C. The accuracy at 3.0 T for the $\text{Cu}_{0.35}\text{Zn}_{0.65}\text{Fe}_2\text{O}_4$ ferrite is similar to the accuracy obtained at 1.5 T with micrometer-sized metallic Gd particles [18], as mass magnetization for both compounds drops at almost the same rate. However, a significant difference in the value of the mass magnetization at 310 K, for Gd ($8.3 \text{ A m}^2 \text{ kg}^{-1} \text{ K}^{-1}$) and for the $\text{Cu}_{0.35}\text{Zn}_{0.65}\text{Fe}_2\text{O}_4$ ferrite ($29 \text{ A m}^2 \text{ kg}^{-1} \text{ K}^{-1}$), leads to greater NMR line broadening and dimmer T_2^* -weighted MRI images for the latter.

Micrometer-sized ferrite particles are too large to be used for intravenous injection during medical procedures that require temperature monitoring with MRI. It is generally understood that particles with diameters of 10–100 nm are appropriate for such procedures [51,52]. In addition, further studies must be carried out to better understand the particles' level of toxicity. We do not expect problems such as nanotoxicity that are common in nanoparticle-based contrast agents [53]. However, recent investigations

have shown that iron overload in humans may cause serious pathological changes leading to heart failure or liver or brain dysfunction [54,55]. Further studies are necessary for a comprehensive evaluation of the toxicity of iron oxides. We note, however, that iron-oxide-based ferrites are, in general, biocompatible and offer the possibility for temperature control during MRI-guided thermal treatments. We can envision, however, a variety of medical applications with micrometer-sized ferrite particles. For example, by embedding the large particles in a silicone cap, one can measure the external temperature of a skull during transcranial focused ultrasound procedures avoiding the generation of hot spots [56,57].

Finally, we would like to comment on the composition selection of $\text{Cu}_{1-x}\text{Zn}_x\text{Fe}_2\text{O}_4$ ferrites to work as temperature sensors for clinical scanners operating at different B_0 fields (1.5, 3, and 7 T). This is a multiparameter problem, and our current work sheds some light on it. The three important parameters are (a) the value of magnetization at a given temperature and field, (b) the temperature dependence of magnetization at a given field, and (c) the concentration of magnetic particles in the solution. At a given value of B_0 , by decreasing the concentration of particles in the solution, one may use particles with a smaller content of Zn. On the other hand, for the same concentration of particles with a different composition, our data clearly indicate that one needs to increase the Zn content in $\text{Cu}_{1-x}\text{Zn}_x\text{Fe}_2\text{O}_4$ ferrite particles for scanners operating at higher fields. Specifically, we obtain the same dependence of dM/dT for samples with $x = 0.65$ in a 3-T field and $x = 0.7$ in a 5-T field (data not shown). Increasing the field to 7 T would result in using particles with a composition of $x = 0.73$ to obtain the same dependence of dM/dT . This observation allows one to tailor a selection of the magnetic particles that depends on the temperature range of interest and the strength of the magnetic field B_0 .

ACKNOWLEDGMENTS

We would like to thank the following individuals for their contribution to this project: K. Petersen, K. Smiley, S. Goldman, N. Sorensen, J. Stroud, and Dr. T. Christensen. We would like to especially thank Dr. J. Bultema for the help with the toxicity studies. N. A. A. is grateful to the Government of Saudi Arabia for the financial support under the Saudi Arabian Culture Mission. Contributions to this article by K. F. S., a worker at NIST, an agency of the U.S. Government, are not subject to U.S. copyright.

-
- [1] A. Ramírez-Torres, R. Rodríguez-Ramos, F. J. Sabina, C. García-Reimbert, R. Penta, J. Merodio, R. Guinovart-Díaz, J. Bravo-Castillero, A. Conci, and L. Preziosi, The role of malignant tissue on the thermal distribution of cancerous breast, *J. Theor. Biol.* **426**, 152 (2017).

- [2] Q. Zhao, J. Zhang, R. Wang, and W. Cong, Use of a thermocouple for malignant tumor detection. Investigating temperature difference as a diagnostic criterion, *IEEE Eng. Med. Biol. Mag.* **27**, 64 (2008).
- [3] M. Sund-Levander, C. Forsberg, and L. K. Wahren, Normal oral, rectal, tympanic and axillary body temperature in adult men and women: A systematic literature review, *Scandinavian Journal of caring sciences* **16**, 122 (2002).
- [4] L. McCallum and D. Higgins, Measuring body temperature, *Nurs. Times* **108**, 20 (2011).
- [5] M. Sund-Levander and E. Grodzinsky, Assessment of body temperature measurement options, *Br. J. Nurs.* **22**, 942 (2013).
- [6] A. Copelan, J. Hartman, M. Chehab, and A. M. Venkatesan, High-intensity focused ultrasound: Current status for image-guided therapy, *Seminars in interventional radiology* **32**, 398 (2015).
- [7] P. Wust, B. Hildebrandt, G. Sreenivasa, B. Rau, H. Riess, R. Felix, and P. M. Schlag, Hyperthermia in combined treatment of cancer, *Lancet Oncol.* **3**, 487 (2002).
- [8] V. Rieke and K. Butts Pauly, MR thermometry, *J. Magn. Reson. Imaging* **27**, 376 (2008).
- [9] L. Winter, E. Oberacker, K. Paul, Y. Ji, C. Oezerdem, P. Ghadjar, A. Thieme, V. Budach, P. Wust, and T. Niendorf, Magnetic resonance thermometry: Methodology, pitfalls and practical solutions, *International Journal of Hyperthermia* **32**, 63 (2016).
- [10] D. L. Bihan, J. Delannoy, and R. L. Levin, Temperature mapping with MR imaging of molecular diffusion: Application to hyperthermia, *Radiology* **171**, 853 (1989).
- [11] J. De Poorter, C. De Wagter, Y. De Deene, C. Thomsen, F. Stahlberg, and E. Achten, The proton-resonance-frequency-shift method compared with molecular diffusion for quantitative measurements of two-dimensional time dependent temperature distribution in a phantom, *J. Magn. Reson.* **103**, 234 (1994).
- [12] J. De Poorter, C. De Wagter, Y. De Deene, C. Thomsen, F. Stahlberg, and E. Achten, Noninvasive MRI thermometry with the proton resonance frequency (PRF) method: *In vivo* results in human muscle, *Magn. Reson. Med.* **33**, 74 (1995).
- [13] B. Dennis de Senneville, B. Quesson, and C. T. W. Moonen, Magnetic resonance temperature imaging, *International Journal of Hyperthermia* **21**, 515 (2005).
- [14] N. W. Lutz, A. C. Kuesel, and W. E. Hull, A ¹H-NMR method for determining temperature in cell culture perfusion systems, *Magn. Reson. Med.* **29**, 113 (1993).
- [15] P. Wang, Evaluation of MR thermometry with proton resonance frequency method at 7T, *Quant. Imaging Med. Surg.* **7**, 259 (2017).
- [16] V. Rieke, K. K. Vigen, G. Sommer, B. L. Daniel, J. M. Pauly, and K. Butts, Referenceless PRF shift thermometry, *Magn. Reson. Med.* **51**, 1223 (2004).
- [17] K. Kuroda, Non-invasive MR thermography using the water proton chemical shift, *International Journal of Hyperthermia* **21**, 547 (2005).
- [18] J. H. Hankiewicz, Z. Celinski, K. F. Stupic, N. R. Anderson, and R. E. Camley, Ferromagnetic particles as magnetic resonance imaging temperature sensors, *Nat. Commun.* **7**, 12415 (2016).
- [19] M. Rogosnitzky and S. Branch, Gadolinium-based contrast agent toxicity: a review of known and proposed mechanisms, *Biometals: an international Journal on the role of metal ions in biology, biochemistry, and medicine* **29**, 365 (2016).
- [20] J. H. Hankiewicz, N. Alghamdi, N. M. Hammelev, N. R. Anderson, R. E. Camley, K. Stupic, M. Przybylski, J. Zukrowski, and Z. J. Celinski, Zinc doped copper ferrite particles as temperature sensors for magnetic resonance imaging, *AIP Adv.* **7**, 056703 (2017).
- [21] H. L. Karlsson, P. Cronholm, J. Gustafsson, and L. Möller, Copper oxide nanoparticles are highly toxic: a comparison between metal oxide nanoparticles and carbon nanotubes, *Chemical research in toxicology* **21**, 1726 (2008).
- [22] M. S. Khandekar, N. L. Tarwal, I. S. Mulla, and S. S. Suryavanshi, Nanocrystalline Ce doped CoFe₂O₄ as an acetone gas sensor, *Ceram. Int.* **40**, 447 (2014).
- [23] J. A. Paulsen, A. P. Ring, C. C. H. Lo, J. E. Snyder, and D. C. Jiles, Manganese-substituted cobalt ferrite magnetostrictive materials for magnetic stress sensor applications. *J. Appl. Phys.* **97**, 044502 (2005).
- [24] D. M. Bruls, T. H. Evers, J. A. H. Kahlman, P. J. W. van Lankvelt, M. Ovsyanko, E. G. M. Pelssers, J. J. H. B. Schleipen, F. K. de Theije, C. A. Verschuren, T. van der Wijk, J. B. A. van Zon, W. U. Dittmer, A. H. J. Immink, J. H. Nieuwenhuis, and M. W. J. Prins, Rapid integrated biosensor for multiplexed immunoassays based on actuated magnetic nanoparticles, *Lab Chip* **9**, 3504 (2009).
- [25] Y. Kumar, A. Sharma, and P. M. Shirage, Shape-controlled CoFe₂O₄ nanoparticles as an excellent material for humidity sensing, *RSC Adv.* **7**, 55778 (2017).
- [26] F. Tudorache, Investigations on microstructure, electrical and magnetic properties of copper spinel ferrite with WO₃ addition for applications in the humidity sensors, *Superlattices Microstruct.* **116**, 131 (2018).
- [27] C. Miclea, C. Tanasoiu, C. F. Miclea, I. Spanulescu, M. Cioangher, and C. T. Miclea, Magnetic temperature transducers made from copper based soft ferrite, *Adv. Sci. Technol.* **54**, 62 (2008).
- [28] S. Akther, D. P. Paul, Md. A. Hakim, S. Akhter, S. M. Hoque, and H. N. Das, Magnetic properties of Cu_{1-x}Zn_xFe₂O₄ ferrites with the variation of zinc concentration, *J. Mod. Phys.* **03**, 398 (2012).
- [29] M. Przybylski, J. Żukrowski, I. Harward, and Z. Celiński, Mössbauer spectroscopy study of Al distribution in BaAl_xFe_{12-x}O₁₉ thin films, *J. Appl. Phys.* **117**, 17A501 (2015).
- [30] L. Bordonali, T. Kalaivani, K. P. V. Sabareesh, C. Innocenti, E. Fantechi, C. Sangregorio, M. F. Casula, L. Lartigu, J. Larionova, Y. Guari, M. Corti, P. Arosio, and A. Lascialfari, NMR-D study of the local spin dynamics and magnetic anisotropy in different nearly monodispersed ferrite nanoparticles, *J. Phys. Condens. Matter* **25**, 066008 (2013).
- [31] T. C. Farrar and E. D. Becker, *Pulse and Fourier Transform NMR: Introduction to Theory and Method* (Academic Press, New York, 1971).
- [32] M. Bernstein, K. King, and X. Zhou, *Handbook of MRI Pulse Sequences* (Elsevier, Amsterdam, 2004).
- [33] G. B. Chavhan, P. S. Babyn, B. Thomas, M. M. Shroff, and E. M. Haacke, Principles, techniques, and applications of

- T_2^* -based MR imaging and its special applications, *Radio-graphics* **29**, 1433 (2009).
- [34] S. Qin, F. Liu, I. W. Turner, Q. Yu, Q. Yang, and V. Vegh, Characterization of anomalous relation using the time-fractional Bloch equation and multiple echo T_2^* -weighted magnetic resonance imaging at 7 T, *Magn. Reson. Med.* **77**, 1485 (2017).
- [35] E. J. W. Verwey and E. L. Heilmann, Physical properties and cation arrangement of oxides with spinel structures I. Cation arrangement in spinels, *J. Chem. Phys.* **15**, 174 (1947).
- [36] K. Fabian, V. P. Shcherbakov, and S. A. McEnroe, Measuring the Curie temperature, *Geochem. Geophys. Geosyst.* **14**, 947 (2013).
- [37] S. Akhter, D. P. Paul, S. M. Hoque, M. A. Hakim, M. Hudl, R. Mathieu, and P. Nordblad, Magnetic and magnetocaloric properties of $\text{Cu}_{1-x}\text{Zn}_x\text{Fe}_2\text{O}_4$ ($x = 0.6, 0.7, 0.8$) ferrites, *J. Magn. Magn. Mater.* **367**, 75 (2014).
- [38] H. El. Moussaoui, R. Masrour, O. Mounkachi, M. Hamedoun, and A. Benyoussef, Cation distribution and magnetic interactions in Zn-substituted $\text{Fe}(\text{Cu})\text{Fe}_2\text{O}_4$ ferrites, *J. Supercond. Novel Magn.* **25**, 2473 (2012).
- [39] H. Iida, K. Takayanagi, T. Nakanishi, and T. Osaka, Synthesis of Fe_3O_4 nanoparticles with various sizes and magnetic properties by controlled hydrolysis, *J. Colloid Interface Sci.* **314**, 274 (2007).
- [40] T. Osaka, T. Nakanishi, S. Shanmugam, S. Takahama, and H. Zhang, Effect of surface charge of magnetite nanoparticles on their internalization into breast cancer and umbilical vein endothelial cells, *Colloids Surf. B* **71**, 325 (2009).
- [41] V. U. Patil and R. G. Kulkarni, Magnetic properties of Cu-Zn ferrite investigated by Mössbauer spectroscopy, *Solid State Commun.* **31**, 551 (1979).
- [42] R. G. Kulkarni and V. U. Patil, Magnetic ordering in Cu-Zn ferrite, *J. Mater. Sci.* **17**, 843 (1982).
- [43] D. G. Rancourt, Accurate site populations from Mössbauer spectroscopy, *Nucl. Instrum. Methods Phys. Res., Sect. B* **44**, 199 (1989).
- [44] D. G. Rancourt and J. Y. Ping, Voigt-based methods for arbitrary-shape static hyperfine parameter distributions in Mössbauer spectroscopy, *Nucl. Instrum. Methods Phys. Res., Sect. B* **58**, 85 (1991).
- [45] M. Przybylski (unpublished).
- [46] Z. Zhou, R. Tian, Z. Wang, Z. Yang, Y. Liu, G. Liu, R. Wang, J. Gao, J. Song, L. Nie, and X. Chen, Artificial local magnetic field inhomogeneity enhances T_2 relaxivity, *Nat. Commun.* **8**, 15468 (2017).
- [47] R. J. S. Brow, Distribution of fields from randomly placed dipoles: Free-precession signal decay as result of magnetic grains, *Phys. Rev.* **121**, 1379 (1961).
- [48] D. A. Yablonskiy and E. M. Haacke, Theory of NMR signal behavior in inhomogeneous tissues: The static dephasing regime, *Magn. Reson. Med.* **32**, 749 (1994).
- [49] P. Gillis, F. Moiny, and R. A. Brooks, On T_2 -shortening by strongly magnetized spheres: A partial refocusing model, *Magn. Reson. Med.* **47**, 257 (2002).
- [50] Q. L. Vuong, P. Gillis, and Y. Gossuin, Monte Carlo simulation and theory of proton NMR transverse relaxation induced by aggregation of magnetic particles used as MRI contrast agents, *J. Magn. Reson.* **212**, 139 (2011).
- [51] Wahajuddin S. Arora, Superparamagnetic iron oxide nanoparticles: Magnetic nanoplateforms as drug carrier, *Int. J. Nanomed.* **7**, 3445 (2012).
- [52] M. A. Fortin, *Functional Materials: For Energy, Sustainable Development and Biomedical Sciences*, edited by M. Leclerc and R. Gauvin (De Gruyter, Berlin, 2016).
- [53] G. Liu, J. Gao, H. Ai, and X. Chen, Applications and potential toxicity of magnetic iron oxide nanoparticles, *Small* **9**, 1533 (2013).
- [54] M. Wang, Rong-Rong Liu, Cong-Jun Wang, W. Kang, Gao-Hui Yang, Wu-Ning Zhong, and Yong-Rong Lai, Combined histological and hematological assessment of iron-induced organ damage in a gerbil model of iron overload, *Am. J. Transl. Res.* **7**, 385 (2015).
- [55] E. M. Haacke, N. Y. Cheng, M. J. House, Q. Liu, J. Neelavalli, R. J. Ogg, A. Khanb, M. Ayazb, W. Kirsche, and A. Obenaus. Imaging iron stores in the brain using magnetic resonance imaging, *Magn. Reson. Imaging* **23**, 1 (2005).
- [56] F. A. Jolesz and N. J. McDannold, Magnetic resonance-guided focused ultrasound: A new technology for clinical neurosciences, *Neurol. Clin.* **32**, 253 (2014).
- [57] W. Legon, T. F. Sato, A. Opitz, J. Mueller, A. Barbour, A. Williams, and W. J. Tyler, Transcranial focused ultrasound modulates the activity of primary somatosensory cortex in humans, *Nat. Neurosci.* **17**, 322 (2014).